Ascent and compaction of gas rich magma and the effects of hysteretic permeability

Chloé Michaut [a,*], David Bercovici [a], R. Steve J. Sparks [b]

[a] Department of Geology and Geophysics, Yale University, P.O. Box 208109, New Haven, CT 06520-8109, USA
[b] Department of Earth Sciences, Wills Memorial Building, University of Bristol, Bristol, BS8 1RJ, UK

ARTICLE INFO

ABSTRACT

Gas escape from volcanic conduits plays an important role in eruption dynamics and eruptive cycles. Gas volume fraction influences magma permeability, but permeability is also likely to depend on prior gas volume fraction through a hysteretic relationship. We study how this permeability behavior affects vertical segregation of gas and compaction of ascending magma. Ascent of vesiculated magma leads to compaction profiles in which gas volume fraction and permeability decrease substantially with height. Classical and hysteretic permeability functions can, however, lead to very different permeability profiles. If the magma ascent velocity is small enough, the hysteretic behavior introduces a step in the permeability profile such that a low-permeability plug sits on top of a gas-rich magma and acts as a trap for gases rising from depth. Time-dependent solutions take the form of porosity waves, although in the hysteretic case, gas is more concentrated into a thinner wave for a given amount of gas, leading to more powerful eruptions. This model shows that a highly vesicular magma can change into a degassed magma over a short distance, which has implications for phenomena such as seismicity, ground motion and eruptive behavior.

© 2009 Elsevier B.V. All rights reserved.

1. Introduction

Episodes of dome growth commonly alternate with cycles of explosive eruptions, ground deformation, seismicity and degassing at volcanoes erupting intermediate magmas, such as Soufrière Hills, Montserrat and Mount Pinatubo, Philippines. These explosive events typically have recurrence intervals of a few hours to a few days (Denlinger and Hoblitt, 1999; Druitt et al., 2002; Voight et al., 1999; Formenti et al., 2003). Previous studies on eruptive cycles show that, following gas-rich explosive eruptions, a dense, stiff and impermeable plug forms rapidly at the top of the conduit (Voight et al., 1999; Clarke et al., 2007). This plug contributes to pressurize the conduit and chamber by preventing open-system degassing of the magma at depth and allowing gas pressure to rise. Increasing pressure under the plug eventually causes extrusion of magma or an explosive eruption which initiates a new cycle (Voight et al., 1999; Connor et al., 2003). The timescale of plug formation is too short to be explained by conductive cooling of magma, and is better explained by rheological stiffening of a degassing and crystallizing magma (Voight et al., 1999) as well as a mechanism to make the plug impermeable and prevent gas escape.

The efficiency of gas escape from magma plays a crucial role in eruption dynamics. In the permeable foam model (Taylor et al., 1983; Jaupart, 1998; Melnik and Sparks, 1999), gas bubbles in ascending magma

become interconnected and gas escapes either vertically through the permeable magma or laterally toward the conduit walls. Gonnermann and Manga (2003) suggest that a highly permeable fractured region develops at the walls along which gas can escape. Under the magma column weight, the mixture of magma and gas deforms viscously, magma compacts, i.e. it collapses and expels gas, and gas segregates due to its buoyancy. However, little attention has been given to the combined effects of gas segregation and magma compaction on eruption dynamics.

Compaction of partially molten rocks has been extensively studied (McKenzie, 1984, 1987; Spiegelman, 1993). Melt segregation by compaction and Darcy flow has been shown to occur through propagating magmons or solitary waves (Scott and Stevenson, 1984; Spiegelman, 1993; Rabinowicz et al., 2002).

Here we adapt the theory of magma compaction and melt segregation (Scott and Stevenson, 1984; McKenzie, 1987) although the volume fraction of gas in magma is larger than the fraction of melt in mantle rocks. Gas volume fraction in magma varies from 0 to 70%, above which fragmentation and turbulent flow occur, thus somewhat different physics has to be considered. Over this large range of gas fractions, magma permeability is likely to exhibit complex behavior. In particular, permeability might depend on the history of porosity interconnectedness in that isolated bubbles persist from low to moderate porosity, while interconnected networks remain from high to low porosity, thereby leading to a hysteretic permeability-porosity relation. Such hysteretic behavior has been suggested by measurements on natural and experimental samples (Rust and Cashman, 2004; Takeuchi et al., 2005).

In this study, we account for the effect of hysteretic permeability on gas and magma separation; we show that, in contrast to a classic
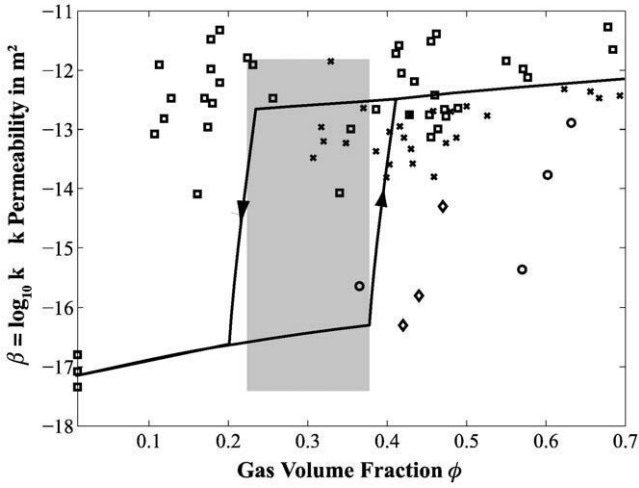
Fig. 1. Porosity/permeability data; crosses from Klug and Cashman (1996), diamonds from Takeuchi et al., (2005), circles from Eichelberger et al. (1986), squares from Saar and Manga (1999). The shaded area corresponds to the percolation threshold predicted by theory and numerical experiments (Blower, 2001). A hysteretic permeability/ porosity relationship is proposed here following Rust and Cashman (2004) and is represented by the arrows.

permeability function, compaction and segregation can concentrate gas into thin but highly vesicular zones.

2. Magma permeability

We define porosity or gas volume fraction as the volume fraction of gas in the form of bubbles or pores, excluding gas dissolved in magma. The relationship between magma porosity and permeability is crucial for understanding magma compaction; it is, however, potentially complex. To fit their experimental data, Eichelberger et al. (1986) and Westrich and Eichelberger (1994) proposed an abrupt increase in permeability at a threshold porosity below which the magma is impermeable. But, discrepancies in experimental results on different natural samples, in particular at low porosity, led Rust and Cashman (2004) to suggest a hysteretic permeability-porosity relationship.

Significant hysteresis could reconcile observations on natural samples and recent experiments showing both high and low permeability values below 65% porosity. Percolation theory and numerical experiments also predict the existence of a percolation threshold close to 30% porosity, below which permeability is almost zero (Sahimi, 1994; Blower, 2001). Above 30% vesicularity, most measurements on natural samples of dacitic to rhyolitic pumices show a gradual increase in permeability k with vesicularity ϕ, such that magma permeability can be estimated using $k = k_0\phi^n$, where k_0 is a reference permeability and $2 \leq n \leq 4$ (Klug and Cashman, 1996; Melnik and Sparks, 2002) (Fig. 1). However, permeability measurements on synthetic samples of dacitic pumice and on natural rhyolite dome samples reveal very low permeability values at high vesicularity up to 40–50% (Takeuchi et al., 2005; Eichelberger et al., 1986). In contrast, analyses on basaltic andesite flows and scoria samples have relatively high permeability at gas volume fractions as low as 5 to 10% (Saar and Manga, 1999).

The cause for the inferred hysteresis is that bubble expansion and collapse induce different pore structure (Rust and Cashman, 2004) (Fig. 1). Indeed, observations show that pores or bubble geometries are very different depending on gas fraction, flow dynamics, and degassing history. Gas exsolution is manifested in the nucleation and growth of bubbles as magma decompresses. Initially, at low porosity, bubbles are isolated and the magma has a small permeability; phase separation is limited to ascent of bubbles through magma. According to percolation theory, once bubble fraction exceeds a threshold of ~30%, interconnectedness is pervasive (Sahimi, 1994; Blower, 2001;

Takeuchi et al., 2005) and the magma becomes highly permeable. Alternatively, with an initial high porosity, pores form an interconnected network. With degassing and/or compaction, the reduction in porosity is not the reverse of vesiculation because elongated pores can remain interconnected and significant permeability can persist to low porosity. When gas volume fraction becomes low, interconnected pores become too thin to sustain their structure against surface-tension induced pinching, and separate into isolated gas bubbles with an associated drop in permeability. This hysteretic effect is likely to be important for magma ascent in a conduit because volatile exsolution, degassing and compaction cause porosity to encompass the whole range of values at which hysteresis occurs.

To investigate the effects of both hysteretic and classic permeability on magma and gas separation, we use the following permeability-porosity relationship:

$$\phi = A\beta^2 \times exp^{-\left(\frac{\beta - b_1}{\Delta\beta}\right)^2} + 10^{\frac{\beta - b_2}{2}} \tag{1}$$

where $\beta = \log_{10} k$, and A, b_1, b_2 and $\Delta\beta$ are constants. We formulated (1) to capture either hysteretic or standard behavior, where the hysteresis magnitude is characterized by one parameter, A. For $A = 0$, (1) recovers the classic permeability-porosity function $k = k_0\phi^2$, with $k_0 = 10^{b_2}$. The parameters b_1, b_2, $\Delta\beta$ are fixed such that $k(\phi)$ matches the permeability-porosity trend indicated by the available measurements (Rust and Cashman, 2004) for different values of A (Figs. 1 and 2). We use $\Delta\beta^2 = 0.5$, $b_1 = -14.5$, $b_2 = -12$.

In the classic case ($A = 0$), permeability gradually increases with porosity (Fig. 2). For the other cases of Fig. 2, permeability undergoes hysteresis with two possible branches. The jump to the high-permeability branch corresponds to the percolation threshold; whereas the jump to the low-permeability branch represents pore pinching. Permeability values on the intermediate branch are forbidden since they describe unphysical behavior by which permeability decreases for increased porosity. Both the amplitude of the hysteresis and the value of ϕ at the percolation threshold increase with increasing A. For $A = 5 \times 10^{-4}$, there is little hysteresis but permeability displays a rapid transition at low porosity, associated
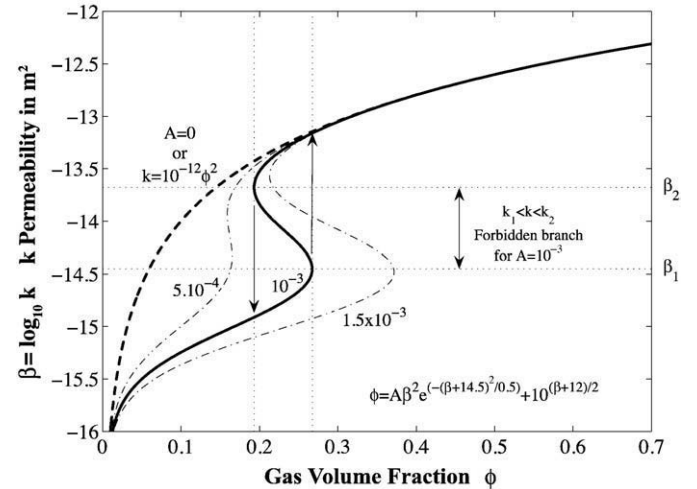
Fig. 2. Different magma permeability functions described by Eq. (1) with varying A (values indicated on the graph). $\beta = \log_{10}k$, with k permeability, is represented as a function of ϕ. In Eq. (1), we use $b_1 = -14.5$, $b_2 = -12$, $\Delta\beta^2 = 0.5$. $A = 0$ (dashed line) is a classic relationship also written as $k = 10^{-12}\phi^2$. Permeability is hysteretic in all three other cases. Both the hysteretic character and the percolation threshold increases with A. In the case $A = 10^{-3}$, values of k between k_1 and k_2 are forbidden: when ϕ increases from 0 to ~0.268, k increases from 0 to $k_1 = 10^{-14.45}$ m²; as ϕ increases further, k jumps to the high-permeability branch. When ϕ decreases from 0.7 to ~0.193, k decreases from $10^{-12.32}$ to $k_2 = 10^{-13.68}$ m², after which it jumps to the low-permeability branch. Dotted lines indicate the values of β and ϕ at which the jumps occur, for $A = 10^{-3}$.

with the percolation threshold. In Sections 4 and 5 we use $A = 10^{-3}$ for which the hysteresis is significant; we examine the effect of different values of A in Section 5.

3. One-dimensional flow of magma and gas

We investigate the basic physics of compaction of a gas-rich magma with hysteretic permeability as it ascends to the surface. Our simple 1-D model does not account for gas exsolution and compressibility. These attributes would play important roles only at shallow depths and introduce extra complexity. Compressibility is not important over the length scales in which compaction occurs (Appendix B), and exsolution is assumed to have occurred below $z = 0$. Nevertheless, we later qualitatively discuss their influences on the eruption/compaction process. Magma and gas are assumed to be injected at the base of a semi-infinite half-space after which the mixture undergoes compaction and phase separation while ascending. Viscous drag from the conduit walls has little influence on the results (Appendix C).

Following the two-phase model of Bercovici et al. (2001), Ricard et al. (2001) and Bercovici and Ricard (2003), we write the 1-D continuity equations for gas and magma:

$$\frac{\partial (1-\phi)}{\partial t} + \frac{\partial}{\partial z}((1-\phi)w_m) = 0 \tag{2}$$

$$\frac{\partial \phi}{\partial t} + \frac{\partial}{\partial z}\left(\phi w_g\right) = 0 \tag{3}$$

where z is the vertical coordinate, t is time, w is vertical velocity, subscripts g and m stands for gas and magma. The force balance equations are:

$$0 = -\phi \frac{\partial P_g}{\partial z} - \phi \rho_g g + c(\phi)\Delta w \tag{4}$$

$$0 = -(1-\phi)\frac{\partial P_m}{\partial z} - (1-\phi)\rho_m g + \frac{4}{3}\mu_m \frac{\partial}{\partial z}\left((1-\phi)\frac{\partial w_m}{\partial z}\right) \tag{5}$$
$$- c(\phi)\Delta w + \Delta P \frac{\partial \phi}{\partial z}$$

where P is pressure, μ viscosity, ρ is density and $\Delta q = q_m - q_g$ for any quantity q. The factor $(1-\phi)$ in the term involving magma viscosity represents the dependence of the effective mixture viscosity on gas volume fraction. This dependence may be more complicated (Llewellin and Manga, 2005). The pressure difference between phases drives isotropic compaction of a permeable matrix (e.g., magma pressure in excess of gas pressure will squeeze out gas in all directions).

Following Bercovici and Ricard (2003), one-dimensional isotropic compaction in a viscous mixture without surface tension is given by:

$$\Delta P = -\frac{K\mu_m}{\phi}\frac{\partial w_m}{\partial z} \tag{6}$$

where K accounts for grain geometry and is $O(1)$; for simplicity we use $K = 4/3$.

The Darcy drag coefficient c is given by:

$$c(\phi) = \frac{\mu_g \phi^2}{k(\phi)} \tag{7}$$

where $k(\phi)$ is given by Eq. (1) (McKenzie, 1984; Spiegelman, 1993; Bercovici et al., 2001).

Subtracting $(1-\phi) \times$ Eq. (4) from $\phi \times$ Eq. (5), and eliminating ΔP using Eq. (6), we obtain:

$$\frac{4}{3}\frac{\partial}{\partial z}\left(\frac{1-\phi^2}{\phi}\frac{\partial w_m}{\partial z}\right) - (1-\phi)\frac{\Delta\rho g}{\mu_m} - \frac{\mu_g}{\mu_m}\frac{\phi}{k(\phi)}\Delta w = 0 \tag{8}$$

Gas segregation is controlled by three different processes, corresponding to the terms on the left of Eq. (8): (1) the viscous resistance of magma to compaction, (2) gas buoyancy and (3) the resistance to gas percolation through magma (Darcy flow).

4. Steady-state compaction profiles

4.1. Model

We consider the ascent of gas-rich magma at constant velocity. We assume that exsolution of gas is complete and rapid such that little separation and compaction occur below $z = 0$ where $w_m = w_g = W$. Phase segregation starts at the base of the half-space where $\phi = \phi_i$. In steady-state, Eqs. (2) and (3) give $w_m = \frac{1-\phi_i}{1-\phi}W$ and $\Delta w = \frac{\phi - \phi_i}{\phi(1-\phi)}W$. Using the expressions for w_m, Δw and Eq. (7), Eq. (8) gives, with $\Phi' = \frac{d\phi}{dz}$:

$$\frac{d}{dz}\left(\frac{1+\phi}{(1-\phi)\phi}\Phi'\right) = \frac{3\Delta\rho g}{4W\mu_m}\frac{1-\phi}{1-\phi_i} + \frac{3\mu_g}{4\mu_m}\frac{(\phi - \phi_i)}{k(\phi)(1-\phi)(1-\phi_i)}. \tag{9}$$

As $z \to \infty$, compaction is complete, gas segregation is controlled by the balance between Darcy flow and gas buoyancy, and we assume $\Phi' \to 0$ and $\Phi'' \to 0$. The porosity at infinity ϕ_∞ is thus given by:

$$\phi_\infty - \phi_i + (1-\phi_\infty)^2 B\frac{k(\phi_\infty)}{k_0} = 0 \tag{10}$$

where $B = \frac{\Delta\rho g k_0}{\mu_g W}$ is a ratio between a characteristic velocity for phase segregation $\Delta\rho g k_0/\mu_g$ and an ascent velocity W. The term involving B in Eq. (10) is always positive, and hence $\phi_\infty < \phi_i$. The solution of Eq. (10) is determined by substituting $\phi(k)$ from Eq. (1) into Eq. (10) to find k_∞ for which $\phi_\infty = \phi(k_\infty)$. In the case of the hysteretic function, if k_∞ is on the forbidden branch ($k_1 < k_\infty < k_2$, Fig. 2), then no steady-state solution exists. In the classic case ($A = 0$), solutions exist for any value of B. In both cases, the smaller the ascent velocity W and the larger the gas buoyancy (i.e. the larger B) then the easier it is for gas to segregate, leading to smaller ϕ_∞. In contrast, for larger total ascent velocity (i.e. the smaller B), gas segregation becomes more difficult, and ϕ_∞ is larger.

4.2. Mathematical analysis

The solution of the system over multivalued and discontinuous hysteretic functions requires special consideration. Integration of Eq. (9) between ϕ and ϕ_∞ gives:

$$\Phi' = \pm\left(\frac{2}{k_0 \nu(1-\phi_i)}\right)^{1/2}\frac{(1-\phi)\phi}{(1+\phi)}$$
$$\times \left[B\left(\phi - \phi_\infty + \log\frac{\phi}{\phi_\infty}\right) + \int_{\phi_\infty}^{\phi}\frac{k_0}{k(\phi)}\frac{(1+\phi)(\phi-\phi_i)}{\phi(1-\phi)^2}d\phi\right]^{1/2} \tag{11}$$

where $k_0 = 10^{b_2}$, $\nu = 4\,\mu_m/3\,\mu_g$.

For $A = 0$ in (1), i.e. $k = k_0\phi^2$, an analytical solution exists for any value of B and ϕ_i (Appendix A). For $A = 10^{-3}$, the integral is calculated numerically. We consider that magma ascending past $z = 0$ has already exsolved its gas and is thus at a high porosity and permeability; ϕ_i is initially large, such that $k > k_2$, and thus on the high-permeability branch of the hysteretic curve (Fig. 2).
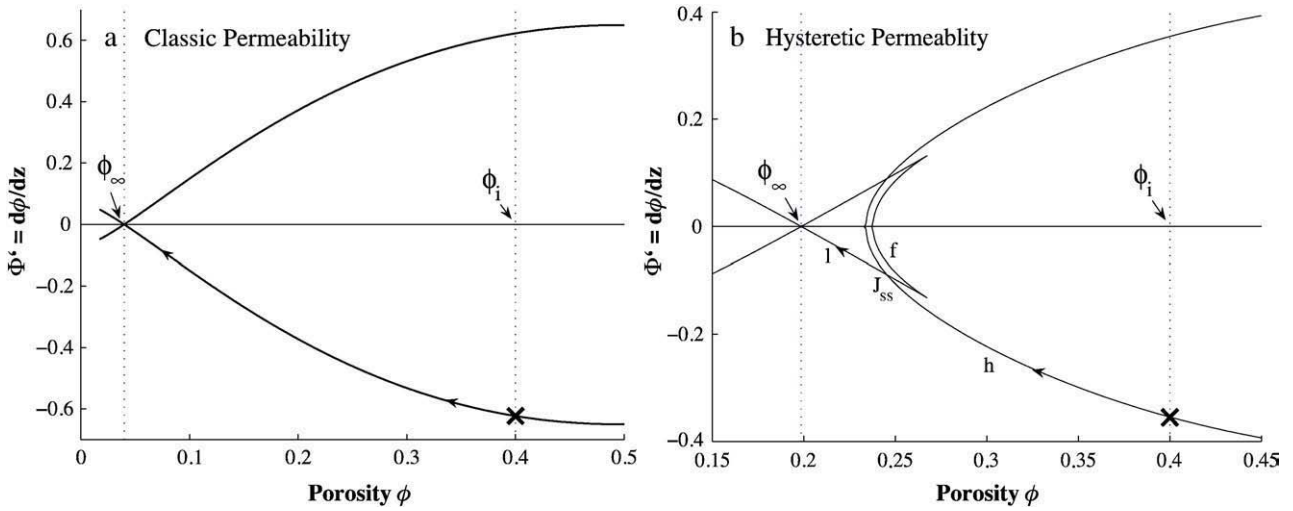
Fig. 3. Vertical derivative of gas volume fraction ϕ as a function of ϕ in steady-state, with $\phi_i = 0.4$, $B = 245.25$, $v = 1.33 \times 10^{14}$, a) classic permeability, b) hysteretic permeability. The initial condition is indicated by the cross on both graphs. Note the jump from the high permeability branch (h) to the low permeability one (l) in the hysteretic case in J_{ss}. Vertical dotted lines show the porosity values initially and at infinity.

Solutions for Φ' from Eq. (11) are shown as a function of ϕ on Fig. 3a and b respectively for the classic and hysteretic cases. The porosity ϕ decreases from ϕ_i, as magma compacts and gas escapes, thus $\Phi' < 0$, which corresponds to the negative solutions in both cases (Fig. 3). Positive values of Φ' do not represent possible trajectories.

In the classic case ($A = 0$), ϕ decreases from ϕ_i gradually following $\Phi' < 0$ path to reach ϕ_∞ (Fig. 3a).

In the hysteretic case, $\Phi'(\phi)$ has 3 different branches which do not all represent possible paths for ϕ as a function of z (Fig. 3b). The first branch, which is allowed, starts at large ϕ and decreases with $\Phi' < 0$; it represents the high-permeability branch of Fig. 2 and is denoted by "h" on Fig. 3b. The second branch, denoted by "f", starts at $\Phi' = 0$ and ends at the apex where $\phi = \phi(k_1)$; this branch is disallowed because it is associated with the forbidden branch on Fig. 2. The last branch, denoted by "l", represents the low-permeability branch on Fig. 2 and is allowed; it goes from the apex where $\phi = \phi(k_1)$ and decreases to ϕ_∞ where $\Phi' = 0$.

Starting from ϕ_i on the high-permeability branch "h" with $\Phi' < 0$, ϕ could decrease along the branch and reach $\Phi' = 0$ where the high-permeability branch with $\Phi' > 0$ is also allowed (ϕ increases with $\Phi' > 0$); but ϕ_∞ could never be reached in that case, which is not permissible. The jump from the high to the low-permeability branch is thus the only possible path from ϕ_i to ϕ_∞ with ϕ and Φ' being continuous. The porosity and permeability profiles as a function of height are thus calculated by integration along this path.

Although ϕ_∞ and $d\phi/dz$ vary with B, ν and ϕ_i, when permeability is hysteretic and B is large enough such that ϕ_∞ is on the low-permeability branch, $\Phi' = d\phi/dz$ always shows the same structure, with 3 branches, and only one possible path from ϕ_i to ϕ_∞ that includes a jump from the high to the low-permeability branch.

4.3. Steady-state results

The porosity profile $\phi(z)$ is determined by integration of $d\phi/dz$ along the path described in Section 4.2, such that ϕ decreases continuously from ϕ_i to ϕ_∞, and $\Phi' = \frac{d\phi}{dz}$ is continuous. In the hysteretic case, this consideration leads to a jump from the high to the low-permeability branch, i.e. a step in permeability, which occurs at J_{ss} on Figs. 3b and 5.

Numerical integration of Eq. (11) gives ϕ as a function of z. For standard permeability function ($A = 0$), we get a classic compaction profile with the porosity decreasing with height (Fig. 4). In the case shown, B is large and so both ϕ_∞ and k_∞ are small. The steady-state

profile for the hysteretic case ($A = 10^{-3}$) is shown by comparison for the same values of B and ϕ_i (Fig. 4). For both functions the values of k_∞ given by Eq. (10) are very similar, but the corresponding value of ϕ_∞ is larger for the hysteretic function.

Porosity and permeability decrease significantly over a distance called the compacting layer. Above that layer, the term representing magma deformation (compaction) is negligible in Eq. (8); the porosity remains practically constant and tends to its value at $z \to \infty$. The compacting layer has a very similar thickness in both the classic and hysteretic cases (Fig. 4). Eq. (11) shows that $d\phi/dz$ decreases, i.e. the compacting layer thickness increases, when B decreases and $\nu = 4\,\mu_m/3\,\mu_g$ increases. Thus, the larger the ascent velocity W and magma viscosity μ_m and the smaller the reference permeability k_0, the thicker the compacting layer. For this example, the compacting layer is about 2 m thick using $B = 245.25$, and $\nu = 1.33 \times 10^{14}$, which could correspond to a velocity $W = 10^{-5}$ m s^{-1}, i.e. a very small flux of magma and gas, using $\Delta\rho = 2500$ kg m^{-3}, $g = 9.81$ m s^{-2}, $k_0 = 10^{-12}$ m^2, $\mu_g = 10^{-5}$ Pa s and $\mu_m = 10^9$ Pa s. Compaction occurs over a thickness
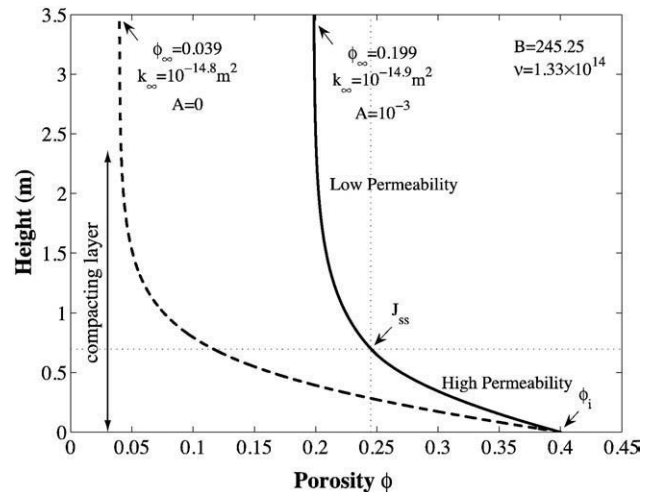
Fig. 4. Steady-state compaction profiles, i.e. porosity as a function of height, in the classic (dashed line), and hysteretic case (solid line), for $\phi_i = 0.4$, $B = 245.25$, $\nu = 1.33 \times 10^{14}$. In the hysteretic case, the permeability jumps from a high to a low value at J_{ss}. Dotted lines indicate height and porosity values at which the jump in permeability occurs. The compacting layer is the layer over which porosity varies significantly; its thickness is very similar for both the hysteretic and the classic cases.

much smaller than the height of a volcanic conduit, which is typically of several km. Using the same values for the parameters W, k_0, $\Delta\rho$ and μ_g and varying μ_m from 10^6 to 10^{11} Pa s, the compacting layer thickness varies from ~10 cm to 35 m for both the classic and hysteretic permeability. In the classic case, using the same parameters as above with $\mu_m = 10^9$ Pa s, but varying W from 10^{-6} to 10^{-3} m s^{-1}, the thickness varies from ~1 to 35 m. Our assumption of a semi-infinite medium is thus justified, as is our assumption that gas exsolution and compressibility can be neglected over these short compacting lengths.

Note that for large values of W greater than about 10^{-2} m s^{-1}, gas segregation and magma compaction are inefficient and no phase separation occurs; ϕ_∞ is then very close to ϕ_i.

As long as $k_\infty > k_2$, both standard and hysteretic functions are very similar and the compaction profiles (i.e. both porosity and permeability profiles) do not differ significantly from each other. But, for large values of B, such that $k_\infty < k_1$, k jumps to the low-permeability branch in the case of the hysteretic function, which causes a much larger ϕ_∞ and a different overall porosity profile.

In the classic case, the permeability decreases gradually from $k_i = 10^{-12.8}$ m^2 to $k_\infty = 10^{-14.9}$ m^2 without a step (Fig. 5). However, for the hysteretic case, the permeability profile shows a step, with a high-permeability layer below a low-permeability magma column. Permeability decreases gradually from k_i at $z = 0$ to $10^{-13.3}$ m^2, jumps at J_{ss} to a much lower value of $10^{-14.7}$ m^2, and then decreases gradually to k_∞ (Figs. 3b and 5).

In summary, for both permeability functions, the steady-state porosity profile shows that compaction of a gas-rich magma ascending at velocity W leads to a decrease in gas volume fraction with height. In the classic case, permeability decreases gradually with height. But the steady-state profile for the hysteretic function is characterized by a step in permeability with a low-permeability plug on top, assuming W is small enough.

Such a permeability profile might influence the eruption dynamics if more gas is suddenly supplied at the base. In contrast to a classic compaction profile showing a gradual decrease in permeability, the step in permeability might cause gas to concentrate at depth and thus gas pressure to accumulate to explosive (fracture strength) levels.

5. Time-dependent gas transport

The time-dependence of the compacting system for both permeability functions is here investigated by looking at solitary wave solutions to the Eqs. (2), (3) and (8). We consider a mixture of magma
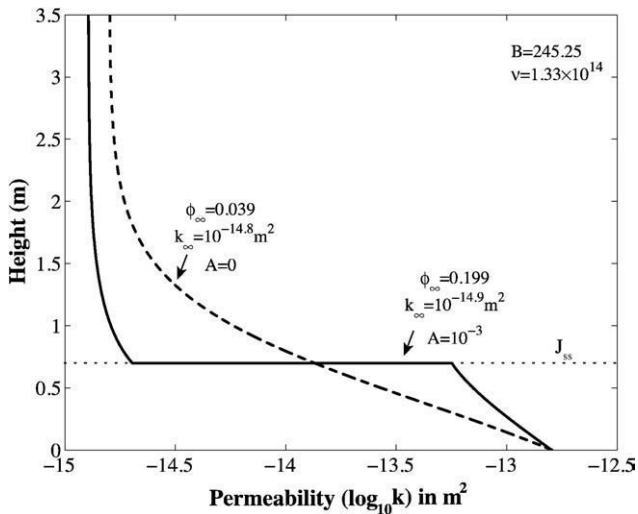

Fig. 5. Steady-state profiles for the permeability as a function of height, in the classic (dashed line), and hysteretic case (solid line), for $\phi_i = 0.4$, $B = 245.25$, $v = 1.33 \times 10^{14}$. Note the jump from high to low permeability values in the hysteretic case at J_{ss}.

and gas with a low reference porosity $\phi_0 = 0.1$, such that magma permeability is low, and study how a pulse of gas is transported through the magma for the different porosity-permeability functions.

Although we have shown that gas exsolution is unlikely to be important over the short distances of a compacting layer, once a low-permeability plug starts to develop, gas from deeper in the conduit will exsolve and flux into the compacting region. Gas release may be triggered by magma ascent and decompression, crystallization, injection of water-rich magmas at shallow depth, or pressure transients, caused, for instance, by dome destabilization. When decompression-induced exsolution proceeds almost instantaneously, this deep source of additional gas can be envisaged as an abrupt pulse of gas. Our analysis below thus captures how a deep pulse of gas can propagate into a low-permeability magma.

5.1. Mathematical analysis

We assume that the additional gas is transported through a single-wave whose shape and velocity are to be determined. Hence, all dependent variables follow a propagating wave solution, e.g. $\phi = \phi(\eta)$ where $\eta = z - ut$ and u is the wave velocity to be determined. We non-dimensionalize Eqs. (2) and (8) using the compaction length scale $\delta = \left(\frac{4\mu_m k_0}{3\mu_g}\right)^{1/2}$ and a characteristic time $\tau = \frac{\delta\mu_g}{k_0\Delta\rho g}$, and express the time and vertical derivatives in terms of derivatives in η. The sum of Eqs. (2) and (3) gives the mean mixture velocity $\phi w_g + (1-\phi)w_m = w$. In the refererence frame of the mean flow, i.e. $\bar{w} = 0$, we have:

$$w_m = -\frac{u\phi + C}{1 - \phi} \tag{12}$$

with C a constant to be determined. Using Eq. (12) in the dimensionless form of Eq. (8) we find:

$$0 = -(u + C)\frac{d}{d\eta}\left(\frac{1+\phi}{\phi(1-\phi)}\frac{d\phi}{d\eta}\right) - (1-\phi) + 10^{b_2 - \beta}\frac{u\phi + C}{1 - \phi} \tag{13}$$

where we have used Eq. (1) in which $k_0 = 10^{b_2} = 10^{-12}$ m^2. Eq. (13) can be recast as:

$$0 = \frac{d^2}{d\eta^2}\left(\log\frac{\phi}{(1-\phi)^2}\right) - \frac{1}{u+C}\left(-(1-\phi) + 10^{b_2 - \beta}\frac{u\phi + C}{1 - \phi}\right). \tag{14}$$

In the case of a single pulse wave we assume that as $\eta \to \infty$, $\phi \to \phi_0$, $\frac{d\phi}{d\eta} \to 0$, $\frac{d^2\phi}{d\eta^2} \to 0$ and $\beta \to \beta_0$, and the flow is controlled by the balance between buoyancy and Darcy drag, which gives:
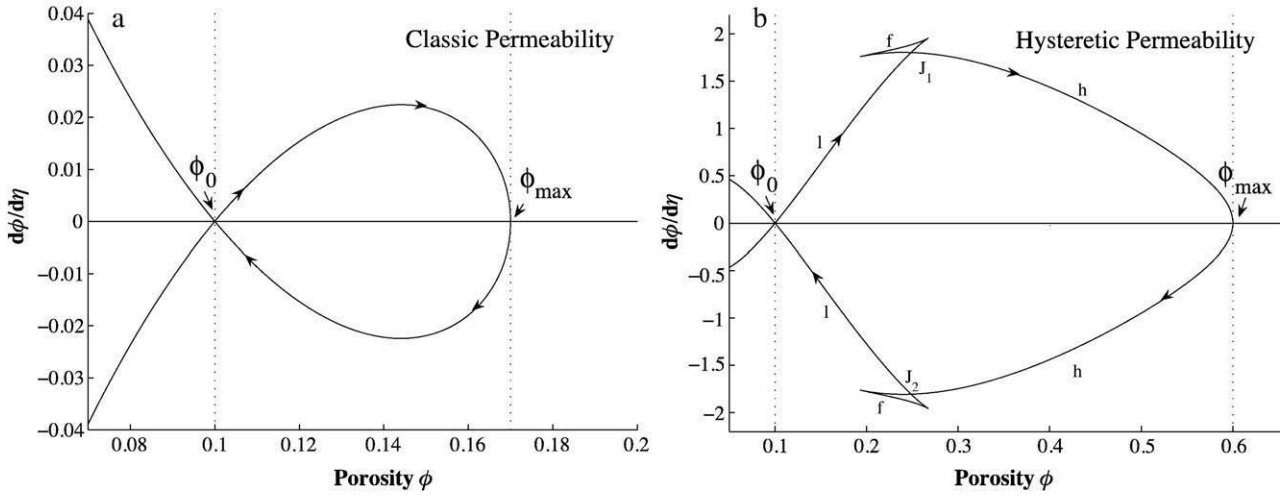
$$C = (1 - \phi_0)^2 10^{\beta_0 - b_2} - u\phi_0. \tag{15}$$

Integrating $\frac{d}{d\eta}\left(\log\frac{\phi}{(1-\phi)^2}\right) \times$ Eq. (14) between ϕ_0 and ϕ or β_0 and β we obtain:

$$\left(\frac{d\phi}{d\eta}\right)^2 = \frac{\phi^2(1-\phi)^2}{(1+\phi)^2}\frac{2}{u+C} \tag{16}$$

$$\times \int_{\beta_0}^{\beta}\left(-\frac{1+\phi}{\phi} + 10^{b_2 - \beta}\frac{(u\phi + C)(1+\phi)}{(1-\phi)^2\phi}\right)\frac{d\phi}{d\beta}d\beta$$

where

$$\frac{d\phi}{d\beta} = 2A\beta exp^{-\frac{(\beta - b_1)^2}{\Delta\beta^2}}\left(1 - \beta\frac{\beta - b_1}{\Delta\beta}\right) + \frac{log10}{2}10^{(\beta - b_2)/2}. \tag{17}$$

Fig. 6. Derivative of gas volume fraction ϕ with respect to η represented as a function of ϕ in the solitary wave case. a) classic permeability, with $\phi_0 = 0.1$ and $\phi_{max} = 0.17$, b) hysteretic permeability with $\phi_0 = 0.1$ and $\phi_{max} = 0.6$. The additional volume of gas transported by the wave are equal in both cases. Note the jumps in permeability from the low (l) to the high branch (h) in J_1 and vice versa in J_2 in the hysteretic case. Dotted lines indicate values of ϕ_0 and ϕ_{max}.

The wave velocity u is determined such that at $\eta = 0$, ϕ reaches its maximum value ϕ_{max} or $\beta = \beta_{max}$ in which case $\frac{d\phi}{d\eta} = 0$; this yields:

$$\int_{\beta_0}^{\beta_{max}} \left(-\frac{1+\phi}{\phi} + 10^{b_2 - \beta} \frac{(u\phi + C)(1+\phi)}{(1-\phi)^2 \phi} \right) \frac{d\phi}{d\beta} d\beta = 0. \quad (18)$$

Analytical expressions for $\frac{d\phi}{d\eta}$ and u as a function of ϕ, ϕ_0 and ϕ_{max} are given in Appendix A for the classic permeability-porosity relationship ($A = 0$). For the hysteretic function with $A = 10^{-3}$, these expressions are calculated numerically.

For a solitary wave solution to exist, the right side of Eq. (16) must be positive for $\phi_0 \le \phi \le \phi_{max}$; the curvature of the porosity-permeability function must also be positive such that $k(\phi)$ is concave at $\phi = \phi_{max}$ (Appendix D). In the classic case, no solitary wave solution exists for ϕ_{max} larger than ≈ 0.36 with $\phi_0 = 0.1$ (Appendix A). However, in the hysteretic case, for $\phi_0 = 0.1$ and $A = 10^{-3}$, these conditions are satisfied even for very large values of $\phi_{max} > 0.7$, and as long as ϕ_{max} is larger than ≈ 0.14. Values of $\phi_{max} > 0.7$ are not considered since the conditions for fragmentation are likely to be reached (Sparks, 1978); (Kaminski and Jaupart, 1998), and the bubbly magma fragments into a gas-pyroclast mixture.

As in the steady-state case, the porosity profile is determined such that ϕ and $\frac{d\phi}{d\eta}$ are continuous. The behavior of $\frac{d\phi}{d\eta}$ given by Eq. (16) is shown in Fig. 6 as a function of ϕ, for both the classic case and hysteretic cases, for equivalent gas pulse.

In the classic case, ϕ starts at ϕ_0 and increases gradually along the branch with $\frac{d\phi}{d\eta} > 0$ until it reaches ϕ_{max}. At ϕ_{max}, ϕ decreases gradually to ϕ_0, along the negative branch with $\frac{d\phi}{d\eta} < 0$ (Fig. 6a).

In the hysteretic case, the structure of $\frac{d\phi}{d\eta}$ shows again three branches for each positive or negative solutions (Fig. 6b), which correspond to the three branches of the permeability function (Fig. 2). The branch denoted by "h", for high-permeability, goes from ϕ_{max} to the apex $\phi(k_2)$ and is stable in the clockwise direction (e.g. decreasing from ϕ_{max} to $\phi(k_2)$ for $\frac{d\phi}{d\eta} < 0$ and conversely). The branch denoted by "f" joins the two apices, going from $\phi(k_2)$ to $\phi(k_1)$ and is disallowed because it is associated with the forbidden branch in Fig. 2. The last branch, denoted by "l" for low-permeability, is stable in the clockwise direction and goes from $\phi(k_1)$ to ϕ_0 for $\frac{d\phi}{d\eta} < 0$, and in reverse for $\frac{d\phi}{d\eta} > 0$.

The existence of a solitary wave requires that the gas volume fraction is continuous with η and the shape of the wave is symmetric with respect to $\phi = \phi_{max}$. Only one path of $d\phi/d\eta$ is then possible for the hysteretic case, which gives the shape of the wave by integration. On Fig. 6b, starting from $\phi = \phi_0$, the gas volume fraction increases along the low-permeability branch following the path for $d\phi/d\eta > 0$ shown by the arrows. At J_1, the permeability jumps to the high-permeability branch and the porosity increases towards ϕ_{max} along the branch "h". The porosity decreases again following the symmetric path for $d\phi/d\eta < 0$ and jumps to the low-permeability branch at J_2. Note that starting at ϕ_0, the branch "l" with $\frac{d\phi}{d\eta} > 0$ can be followed to $\phi(k_1)$. At this point the "f" branch is disallowed because it is non-physical and because following it from the "l" to "h" branches requires ϕ to decrease with $d\phi/d\eta > 0$.

5.2. Solitary wave results

Solitary wave solutions for the time-dependent system are shown in Fig. 7. Results are shown for dimensionless quantities, although thickness and time can be redimensionalized by the compaction length $\delta = (4\mu_m k_0 / 3\mu_g)^{1/2}$ and characteristic gas ascent time $\tau = \delta\mu_g / k_0 \Delta\rho g$. Fig. 7 shows the shapes of the single solitary waves (or gas pulses) corresponding to the prescribed integration paths. In the hysteretic case, the thickness of the wave is about $2 \times \delta$, i.e. ~23 m for $\mu_g = 10^{-5}$ Pa s, $\mu_m = 10^9$ Pa s, whence $\delta = 11.5$ m. The wave velocity is
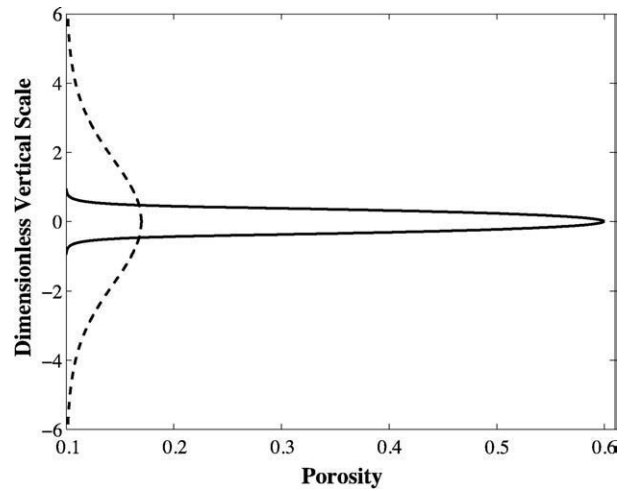
Fig. 7. Solitary wave shapes, i.e. gas volume fraction as a function of dimensionless vertical scale, for a total volume of gas equal to 0.34 in dimensionless unit. The dimensional vertical scale is obtained by multiplying the dimensionless one by the lengthscale $\delta = (4\mu_m k_0 / 3\mu_g)^{1/2}$. Solid line: hysteretic case with $\phi_{max} = 0.6$; dashed line: classic case with $\phi_{max} = 0.17$. $\phi_0 = 0.1$ in both cases.
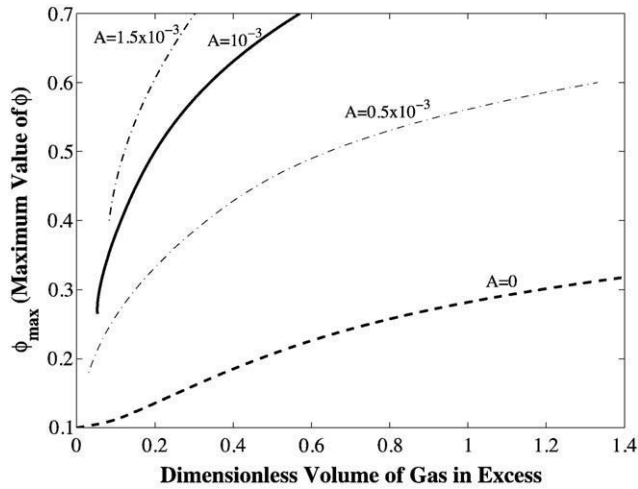
Fig. 8. Maximum value of the gas volume fraction ϕ_{max} within a solitary wave, or gas pulse, as a function of dimensionless total volume of gas transported by the wave, with $\phi_0 = 0.1$ and for different values of the parameter A controlling the hysteresis and percolation threshold (Fig. 2). In the hysteretic cases, we focus on the type of wave showing a jump in permeability, i.e. we choose ϕ_{max} such that it is on the high-permeability branch wherein $\phi_{max} \geq \phi(k_1) \geq 0.268$ for $A = 10^{-3}$ (Fig. 2).

0.016 in dimensionless units, i.e. 4×10^{-5} m s^{-1} for a characteristic velocity $U = k_0 \Delta \rho g / \mu_g = 2.5 \times 10^{-3}$ m s^{-1}. The 1-D additional volume of gas transported by the solitary wave and defined by $\int (\phi - \phi_0) d\eta$ is of 0.34 in dimensionless units, i.e. ~4 m for $\delta = 11.5$ m.

The same additional volume of gas (equal to 0.34) is transported in the classic case for $\phi_{max} = 0.17$, i.e. a porosity only 7% higher than the surrounding porosity ϕ_0. The "classic" wave is much thicker (Fig. 7), approximately ~13 × δ, i.e. ~150 m for $\delta = 11.5$ m, and much faster with a velocity about ten times higher (0.16 in dimensionless unit).

The Darcy flow velocity in the far field is given by $U \frac{k(\phi_0)(1 - \phi_0)}{k_0 \phi_0}$. This velocity is equal to 0.09 U in the classic case, and 0.005 U in the hysteretic case, with $\phi_0 = 0.1$. In both cases, the gas pulse is faster than the background Darcy flow.

For a given gas volume transported by the wave, ϕ_{max} is much larger, and hence the gas is always much more concentrated, for the hysteretic permeability function (Fig. 8). The higher the value of A, the higher the gas fraction at which the permeability step occurs, and the lower the average permeability over the wave. The thickness of the compacting layer increases with the permeability. Thus, the maximum porosity ϕ_{max} increases with increasing A (Fig. 8), for a given volume of gas. Also, the wave velocity for the hysteretic case is always much smaller than for the classic solitary wave. So, for given gas input, the hysteretic function leads to a large concentration in gas and buoyancy.

6. Discussion

Magma permeability depends on the history of gas volume fraction as pore structure evolves. Permeability in vesiculated magma is characterized by hysteretic behavior, such that magma with the same porosity has two possible permeability values. Hysteresis is important for volcanic conduits in which case ascending magma shows a peculiar degassing history. Initially, deep in the conduit, magma exsolves isolated gas bubbles with no connectivity and low permeability. Once a threshold bubble content is achieved, permeability becomes significant and increases, as in the classic case, with increasing porosity. However if gas segregation and/or magma compaction reduces porosity, the permeability is retained provided the processes are fast enough to prevent destruction of pore connectivity.

We have not treated the early stage of vesiculation in which a high permeability and high bubble content arrives in the upper conduit, but

have investigated how such a system subsequently behaves once it passes some arbitrary location where gravitational compaction dominates. A key result is that, in the presence of flow, the compaction profile reverses such that porosity and permeability decreases substantially with height. Steady-state compaction of gas-rich magma supplied at a given velocity leads to classic compaction profiles (McKenzie, 1984, 1987; Ribe, 1985) showing a progressive decrease in gas fraction with height in both the classic and hysteretic cases. But, in the hysteretic case, if the velocity is small enough, the permeability profile shows a step and jumps from a high to a low overlying value, creating a low-permeability plug on top of a highly vesiculated magma.

Rapid decompression of the magma column below a pre-existing plug caused by, for example, dome collapse, leads to volatile exsolution; this induces a gas pulse (Lensky et al., 2008) that potentially rises through the degassed magma as a solitary wave. Our model shows that, for increasingly hysteretic permeability, the gas becomes more concentrated in a thin wave with a much higher maximum porosity and buoyancy than in the classic permeability case, allowing for more expansion at the surface. With expansion, the wave's peak porosity can reach the fragmentation threshold leading to the fracture of the overlying plug and to an explosive eruption. An explosive eruption can then lead to dome collapse and to the initiation of a new cycle of plugging and eruption (Mason et al., 2006).

Compaction is a key process in changing bubble-rich vesiculated magma into degassed magma that forms an impermeable plug behind which gas pressure builds up. For typical silicic magma viscosities and conduit velocities (Sparks, 1997), the compacting layer thickness is tens of centimeters to tens of meters, which is a small fraction of the conduit length, as is consistent with several observations at the Soufriere Hills Volcano (SHV), Montserrat. First, studies of the products of Vulcanian and sub-Plinian explosions at SHV indicate that highly vesicular magma underlies a plug of degassed magma (Robertson et al., 1998; Clarke et al., 2007). The ejecta in these cases have bimodal densities consistent with an abrupt transformation in porosity. In Clarke et al. (2007), clast density increases dramatically from approximately 1000 kg m^{-3} to >2500 kg m^{-3} while the estimated quench pressure decreases only a few MPa at most, which is comparable to a short compacting distance. Plagioclase compositions and water contents of glasses in SHV ejecta indicate that the transformation takes place at 20 to 30 MPa, i.e. $\simeq$ 1 km. Second, seismicity at SHV (Neuberg et al., 2006; Green and Neuberg, 2006) indicates that earthquakes are located at a narrow depth interval suggestive of brittle failure along the conduit margin (Tuffen and Dingwell, 2005). The abrupt transformation from weak vesiculated magma to strong degassed magma provides a preferred location for the nucleation of conduit margin fractures and the location of earthquakes.

Finally, ground deformation recorded by tilt meters at SHV together with episodic shallow seismicity has documented cycles of dome growth and Vulcanian eruptions that can be explained by stick-slip behavior of extruding magma and gas pressure build-up behind a plug of rheologically-stiffened, degassed magma (Voight et al., 1999; Wylie et al., 1999). The cycles are typically several hours in length and far too fast to be explained by forming a plug by cooling. They are also associated with pulses of gas release (Watson et al., 2000). Compactive formation of a strong degassed plug (the stick phase) combined with gas pressure build-up (Lensky et al., 2008) can explain these cycles.

Appendix A. Analytical solutions for the classic permeability function

In steady-state, using $k = k_0\phi^2$, $\Phi' = \frac{d\phi}{dz}$ is given by:

$$\Phi' = \pm\left(\frac{2}{vk_o(1-\phi_i)}\right)^{1/2}\frac{(1-\phi)\phi}{(1+\phi)} \times \left[B \times \left(\phi - \phi_\infty + \log\frac{\phi}{\phi_\infty}\right)\right.$$

$$+ 2(1-\phi_i) \times \left(\frac{1}{1-\phi} - \frac{1}{1-\phi_\infty}\right) + (5\phi_i - 3)\log\frac{(1-\phi)\phi_\infty}{(1-\phi_\infty)\phi}$$

$$\left. + (3\phi_i - 1)\left(\frac{1}{\phi} - \frac{1}{\phi_\infty}\right) + \frac{\phi_i}{2}\left(\frac{1}{\phi^2} - \frac{1}{\phi_\infty^2}\right)\right]^{1/2}.$$
(19)

For $k = k_0\phi^2$, the velocity u of a solitary wave with a flat minimum at $\phi = \phi_0$ and a maximum in $\phi = \phi_{max}$ is given by:

$$u = \left(\frac{M}{2}\left(\phi_{max}^{-2} - \phi_0^{-2}\right) + 3M\left(\phi_{max}^{-1} - \phi_0^{-1}\right)\right. \tag{20}$$

$$- 2M\left((1-\phi_{max})^{-1} - (1-\phi_0)^{-1}\right) + (\phi_{max} - \phi_0)$$

$$\left. + 5M\log\frac{1-\phi_{max}}{1-\phi_0} - (5M-1)\log\frac{\phi_{max}}{\phi_0}\right)$$

$$\times\left(-(1-3\phi_0)\left(\phi_{max}^{-1} - \phi_0^{-1}\right) + 2(1-\phi_0)\right.$$

$$\times\left((1-\phi_{max})^{-1} - (1-\phi_0)^{-1}\right) + \frac{\phi_0}{2}\left(\phi_{max}^{-2} - \phi_0^{-2}\right)$$

$$\left. - (3-5\phi_0)\log\frac{1-\phi_{max}}{1-\phi_0} + (3-5\phi_0)\log\frac{\phi_{max}}{\phi_0}\right)^{-1}$$

where $M = (1-\phi_0)^2\phi_0^2$. The differential equation for the wave shape:

$$\frac{d\phi}{d\eta} = \frac{\phi(1-\phi)}{1+\phi}\frac{\sqrt{2}}{(M+(1-\phi_0)u)^{1/2}} \times \left[-\frac{M-u\phi_0}{2}\left(\phi^{-2} - \phi_0^{-2}\right)\right.$$

$$- (3M + (1-3\phi_0)u)\left(\phi^{-1} - \phi_0^{-1}\right) - (\phi - \phi_0)$$

$$+ 2(M + (1-\phi_0)u)\left((1-\phi)^{-1} - (1-\phi_0)^{-1}\right)$$

$$\left. - (5M + (3-5\phi_0)u)\log\frac{1-\phi}{1-\phi_0} + (5M + (3-5\phi_0)u-1)\log\frac{\phi}{\phi_0}\right]^{1/2}$$
(21)

is integrable. For $\phi_0 = 0.1$ and $\phi_{max} > 0.36$, $d\phi/d\eta$ is imaginary at some ϕ between ϕ_0 and ϕ_{max}, thus $\phi_{max} > 0.36$ is not allowed for $\phi_0 = 0.1$.

Appendix B. Gas compressibility

Here we compare the relative effects of gas segregation and gas compressibility on magma compaction. Gas pressure and density are related by:

$$P_g = \rho_g\frac{RT}{M_g} \tag{22}$$

where $R = 8.314 \text{J K}^{-1} \text{ mol}^{-1}$ is the universal gas constant and M_g the gas molar weight. In steady-state, 1-D mass conservation for the mixture becomes:

$$\frac{d}{dz}((1-\phi)w_m) + \frac{d}{dz}\left(\phi w_g\right) + \phi w_g\frac{d\log\rho_g}{dz} = 0. \tag{23}$$

We assume the vertical gradient in gas pressure obeys to first order:

$$\frac{dP_g}{dz} = -\rho^*g \tag{24}$$

where ρ^* is chosen to represent two end-member cases. In case 1, the gas forms an open interconnected network to the surface, such that the gas pressure gradient is hydrostatic and $\rho^* = \rho_g$. In case 2, the gas forms isolated bubbles and no compaction occurs, and hence both ΔP and $\frac{d^2 w_m}{dz^2}$ are equal to 0 and $\rho^* = \overline{\rho} = \phi\rho_g + (1-\phi)\rho_m$. In both cases, using Eq. (22) in Eq. (24) gives $\frac{d\log\rho_g}{dz} = \frac{1}{H^*}$ where $H^* = \frac{RT}{gM_g}$ in case 1 and $H^* = \frac{RT\rho_g}{gM_g\overline{\rho}}$ in case 2.

A simple scaling of Eq. (23) using $d/dz = 1/\delta$, with δ the compaction length yields:

$$\frac{(1-\phi)w_m}{\delta} + \frac{\phi w_g}{\delta} + \frac{\phi w_g}{H^*} = 0 \tag{25}$$

where δ is likely to be in the range 0.1–10 m for viscous magma (Section 4.3). In case 1 with $\rho^* = \rho_g$, $H^* \simeq 5\times10^4$ m using $T = 1000$ K and $M_g = 18$ g mol^{-1} for water vapor. In case 2 ($\rho^* = \overline{\rho}$), H^* depends mostly on gas density. Following the ideal gas law with $T = 1000$ K, water vapor and carbon dioxide densities are respectively 6.5 and 16 kg m^{-3} at 3 MPa ($\simeq 100$ m depth), and 54 and 132 kg m^{-3} at 25 MPa ($\simeq 1$ km depth in the crust). For these values, H^* varies between $\simeq 122$ m and 1 km. In both cases H^* is much larger than the compaction length δ. Thus gas compressibility can be neglected in Eq. (23) providing that we are situated at a reasonable depth (i.e. deeper than 100 m).

Appendix C. Effect of a narrow conduit

We illustrate the effects of a narrow conduit on magma compaction and gas segregation for the case of a classic permeability and steady-state flow. Similar arguments can be made for the time-dependent regime. We assume conduit flow is unidirectional cylindrical Poiseuille flow. Conservation of momentum in magma becomes:

$$0 = -(1-\phi)\frac{\partial P_m}{\partial z} + \frac{4}{3}\mu_m\frac{\partial}{\partial z}\left((1-\phi)\frac{\partial w_m}{\partial z}\right)$$

$$+ \frac{\mu_m}{r}\frac{\partial}{\partial r}\left(r(1-\phi)\frac{\partial w_m}{\partial r}\right) - (1-\phi)\rho_m g - c(\phi)\Delta w + \Delta P\frac{\partial\phi}{\partial z} \tag{26}$$

where r is radial coordinate. Eqs. (2)–(4) are still valid. Using Eqs. (4), (6), and (7) for the classic permeability case with $k = k_0\phi^2$ and Eq. (26), the same operation as in Section 2 gives:

$$0 = \frac{4}{3}\mu_m\frac{\partial}{\partial z}\left(\frac{1-\phi^2}{\phi}\frac{\partial w_m}{\partial z}\right) + \frac{\mu_m}{r}\frac{\partial}{\partial r}\left(r(1-\phi)\frac{\partial w_m}{\partial r}\right) \tag{27}$$

$$- (1-\phi)\Delta\rho g - \frac{\mu_f}{k_0}\frac{\Delta w}{\phi}$$

where ϕ, w_m and Δw depend on r and z.

In steady-state, $\Delta w = \frac{\phi - \phi_i}{(1-\phi_i)\phi}$, see Section 4.1, where the initial porosity at the base of the column ϕ_i depends on r.

We write w_m and ϕ as the sum of a mean value averaged over the cross-sectional area of the conduit πR^2 plus a deviation which depends on r:

$$w_m(r,z) = \omega_m(z) + \tilde{w}_m(r,z) \tag{28}$$

$$\phi(r,z) = \Phi(z) + \tilde{\phi}(r,z) \tag{29}$$

where areally averaged deviations are zero.

Using Eqs. (28) and (29) in Eq. (27) and taking the areal average gives, to first order:

$$0 = \frac{4}{3}\mu_m \frac{d}{dz}\left(\frac{1-\Phi^2}{\Phi}\frac{d\omega_m}{dz}\right) + \frac{2\mu_m}{R^2}\left[\frac{\partial}{\partial r}\left(r(1-\Phi)\frac{\partial \tilde{w}_m}{\partial r}\right)\right]_0^R \quad (30)$$

$$- (1-\Phi)\Delta\rho g - \frac{\mu_f}{k_0}\frac{(\Phi - \Phi_i)\omega_m}{\Phi^2(1-\Phi_i)}$$

where R is the conduit radius.

The deviation from the mean velocity is approximated by:

$$\tilde{w}_m(r,z) = \omega_m(z)\left(1 - 2\frac{r^2}{R^2}\right) \quad (31)$$

In steady-state, using $\omega_m = \frac{1-\Phi_i}{1-\Phi}\overline{W}$ (see Section 4.1), Eq. (30) gives:

$$\frac{4}{3}\frac{d}{dz}\left(\frac{1+\Phi}{\Phi(1-\Phi)}\frac{d\Phi}{dz}\right) = -\frac{8}{R^2} - \frac{1-\Phi}{1-\Phi_i}\frac{\Delta\rho g}{\mu_m \overline{W}} \quad (32)$$

$$+ \frac{\mu_f}{\mu_m k_0}\frac{(\Phi_i - \Phi)}{\Phi^2(1-\Phi)(1-\Phi_i)}$$

where $\overline{W}$ and Φ_i are the areal averaged velocity and porosity at the column base.

The porosity at infinity Φ_∞ is determined by (see Section 4.1):

$$0 = -\frac{8}{R^2} - \frac{1-\Phi_\infty}{1-\Phi_i}\frac{\Delta\rho g}{\mu_m \overline{W}} + \frac{\mu_f}{\mu_m k_0}\frac{(\Phi_i - \Phi_\infty)}{\Phi_\infty^2(1-\Phi_\infty)(1-\Phi_i)} \quad (33)$$

The drag exerted by the conduit walls on the magma (first term on right side of Eqs. (30) and (33)) assists buoyancy by pulling the magma down and balancing the positive upward drag exerted by the gas on the magma (term $\propto \mu_f/\mu_m$) and facilitates phase separation. The porosity at infinity is smaller when taking into account the effect of conduit walls. But, as shown below, differences are negligible.

Poiseuille flow in cylindrical coordinate gives $\overline{W} = \frac{\Delta P_c}{8L\mu_m}R^2$, where ΔP_c is the chamber overpressure, and $L \simeq 5$ to 10 km is conduit length. The magnitude of the drag exerted by the walls is then given by $\frac{\Delta P_c}{L\mu_m \overline{W}}$, which we compare to $\frac{\Delta\rho g}{\mu_m \overline{W}}$, the magnitude of the buoyancy force. ΔP_c cannot exceed the strength of the surrounding rocks and is typically $\simeq 5$ to 20 MPa (Barmin et al., 2002; Stasiuk et al., 1993). For those values, the magnitude of the drag force exerted by the walls is less than $\simeq 15\%$ of the magnitude of the buoyancy force and can thus be neglected.

Appendix D. Existence of solitary waves

In the reference frame of mean 1-D flow (for which $\overline{w}=0$), we have $\Delta w = w_m/\phi$, which when substituted into Eq. (8), gives:

$$w_m = \frac{4\mu_m}{3\mu_g}k(\phi)\frac{\partial}{\partial z}\left(\frac{1-\phi^2}{\phi}\frac{\partial w_m}{\partial z}\right) - (1-\phi)\frac{\Delta\rho g k(\phi)}{\mu_g} \quad (34)$$

Substituting Eq. (34) into Eq. (2), we obtain, for small ϕ:

$$\frac{\partial\phi}{\partial t} = \frac{4\mu_m}{3\mu_g}\frac{\partial}{\partial z}\left(k(\phi)\frac{\partial}{\partial z}\left(\frac{1-\phi^2}{\phi}\frac{\partial w_m}{\partial z}\right)\right) - \frac{\Delta\rho g}{\mu_g}\frac{\partial k}{\partial\phi}\frac{\partial\phi}{\partial z}. \quad (35)$$

Eq. (35) shows that the nonlinear wave arises from the balance between a dispersion term, first term on the right of Eq. (35), and a nonlinear steepening term, second term on the right of Eq. (35) where $\frac{\Delta\rho g}{\mu_g}\frac{\partial k}{\partial\phi}$ is the nonlinear wave speed. For the second term to allow steepening of the wave, the wave speed has to be an increasing function of ϕ so that wave peaks have higher velocity than wave bases; in this case $\frac{\partial k}{\partial\phi}$ has to increase with ϕ, i.e. $\frac{\partial^2 k}{\partial\phi^2} > 0$.

References

Barmin, A., Melnik, O.E., Sparks, R.S.J., 2002. Periodic behavior in lava dome eruptions. Earth Planet. Sci. Lett. 199, 173–184.

Bercovici, D., Ricard, Y., 2003. Energetics of a two-phase model of lithospheric damage, shear localization and plate-boundary formation. Geophys. J. Int. 152, 581–596.

Bercovici, D., Ricard, Y., Schubert, G., 2001. A two-phase model for compaction and damage. 1. General theory. J. Geophys. Res. 106, 8887–8906.

Blower, J.D., 2001. Factors controlling permeability-porosity relationship in magma. Bull. Volcanol. 63, 497–504.

Clarke, A.B., Stephens, S., Teasdale, R., Sparks, R.S.J., Diller, K., 2007. Petrologic constraints on the decompression history of magma prior to vulcanian explosions at the Soufrière Hills Volcano, Montserrat. J. Volcano. Geotherm. Res. 161. doi:10.1016/j.volgeores.2006.11.007.

Connor, C.B., Sparks, R.S.J., Mason, R.M., Bonadonna, C., Young, S.R., 2003. Exploring links between physical and probabilistic models of volcanic eruptions: the Soufrière Hills Volcano, Montserrat. Geophys. Res. Lett. 30. doi:10.1029/2003GL0117384.

Denlinger, R.P., Hoblitt, R.P., 1999. Cyclic eruptive behavior of silicic volcanoes. Geology 27, 459–462.

Druitt, T.H., Young, S.R., Baptie, B., Calder, C.B.E.S., Clarke, A.B., Cole, P.D., Harford, C.L., Herd, R.A., Luckett, R., Ryan, G., Voight, B., 2002. Episodes of cyclic volcanian explosive activity with fountain collapse at Soufriere Hills Volcano Montserrat. Volcanic processes, products and hazards. Geological Society, London, Memoirs, pp. 281–306.

Eichelberger, J.C., Carrigan, C.R., Westrich, H.R., Price, R.H., 1986. Non-explosive silicic volcanism. Nature 323, 598–602.

Formenti, Y., Druitt, T.H., Kelfoun, K., 2003. Characterisation of the 1997 vulcanian explosions of Soufrière Hills Volcano, Montserrat, by video analysis. Bull. Volcanol. 65, 587–605.

Gonnermann, H.M., Manga, M., 2003. Explosive volcanism may not be an inevitable consequence of magma fragmentation. Nature 426, 432–435.

Green, D., Neuberg, J.W., 2006. Waveform classification of volcanic low-frequency earthquake swarms and its implication at Soufrière Hills Volcano, Montserrat. J. Volcanol. Geotherm. Res. 153, 51–63.

Jaupart, C., 1998. Gas loss from magmas through conduit walls during eruption. Geol. Soc. Lond., Spec. Publ., vol. 145. Physics of Explosive Volcanic Eruptions, pp. 73–90.

Kaminski, E., Jaupart, C., 1998. The size distribution of pyroclasts and the fragmentation sequence in explosive volcanic eruptions. J. Geophys. Res. 103, 29,759–29,779.

Klug, C., Cashman, K.V., 1996. Permeability development in vesiculating magmas: implications for fragmentation. Bull. Volcanol. 100, 58–87.

Lensky, N.G., Sparks, R.S.J., Navon, O., Lyakhovsky, V., 2008. Cyclic activity at Soufrière Hills Volcano, Montserrat: degassing-induced pressurization and stick-slip extrusion. Earth Planet. Sci. Lett. 1 1–1.

Llewellin, E.W., Manga, M., 2005. Bubble suspension rheology and implications for conduit flow. J. Volcanol. Geotherm. Res. 143, 205–217.

Mason, R.M., Starostin, A.B., Melnik, O.E., Sparks, R.S.J., 2006. From vulcanian explosions to sustained explosive eruptions: the role of diffusive mass transfer in conduit flow dynamics. J. Volcanol. Geotherm. Res. 153, 148–165.

McKenzie, D., 1984. The generation and compaction of partially molten rock. J. Petrol. 25, 713–765.

McKenzie, D., 1987. The compaction of igneous and sedimentary rocks. J. Geol. Soc. Lond. 144, 299–307.

Melnik, O.E., Sparks, R.S.J., 1999. Nonlinear dynamics of lava dome extrusion. Nature 402, 37–41.

Melnik, O.E., Sparks, R.S.J., 2002. Dynamics of magma ascent and lava extrusion at soufriere hills volcano, montserrat. The eruption of Soufriere Hills Volcano, Montserrat, from 1995 to 1999. Geol. Soc. Lond., pp. 153–171.

Neuberg, J.W., Tuffen, H., Collier, L., Green, D., Powell, T., Dingwell, D., 2006. The trigger mechanism of low-frequency earthquakes on montserrat. J. Volcanol. Geotherm. Res. 153, 37–50.

Rabinowicz, M., Ricard, Y., Gregoire, M., 2002. Compaction in a mantle with a very small melt concentration: Implications for the generation of carbonatitic and carbonate-bearing high mafic melt impregnations. Earth Planet. Sci. Lett. 203, 205–220.

Ribe, N.M., 1985. The deformation and compaction of partial molten zones. Geophys. J. Int. 83, 487–501.

Ricard, Y., Bercovici, D., Schubert, G., 2001. A two-phase model for compaction and damage. 2. Applications to compaction, deformation, and the role of surface tension. J. Geophys. Res. 106, 8907–8924.

Robertson, R., Cole, P., Sparks, R.S.J., Harford, C., Lejeune, A.M., McGuire, W.J., Miller, A.D., Murphy, M.D., Norton, G., Stevens, N.F., Young, S.R., 1998. The explosive eruption of Soufrière Hills Volcano, Montserrat, West Indies, 17 September, 1996. Geophys. Res. Lett. 25, 3429–3432.

Rust, A.C., Cashman, K.V., 2004. Permeability of vesicular silicic magma: inertial and hysteresis effects. Earth Planet. Sci. Lett. 228, 93–107.

Saar, M.O., Manga, M., 1999. Permeability-porosity relationship in vesicular basalts. J. Geophys. Res. 101, 17,457–17,465.

Sahimi, M., 1994. Applications of percolation theory. Taylor and Francis, Bristol, Pa.

Scott, D.R., Stevenson, D.J., 1984. Magma solitons. Geophys. Res. Lett. 11, 1161–1164.

Sparks, R.S.J., 1978. The dynamics of bubble formation and growth in magmas: a review and analysis. J. Volcanol. Geotherm. Res. 3, 1–37.

Sparks, R.S.J., 1997. Causes and consequences of pressurisation in lava dome eruptions. Earth Planet. Sci. Lett. 150, 177–189.

Spiegelman, M., 1993. Physics of melt extraction: theory, implications and applications. Philos. Trans. R. Soc. London, Ser. A 342, 23–41.

Stasiuk, M.V., Jaupart, C., Sparks, R.S.J., 1993. On the variations of flow rate in non-explosive lava eruptions. Earth Planet. Sci. Lett. 114, 505–516.

Takeuchi, S., Nakashima, S., Tomiya, A., Shinohara, H., 2005. Experimental constraints on the low gas permeability of vesicular magma during decompression. Geophys. Res. Lett. 32. doi:10.1029/2005GL022491.

Taylor, B.E., Eichelberger, J.C., Westrich, H.R., 1983. Hydrogen isotopic evidence of rhyolitic magma degassing during shallow intrusion and eruption. Nature 306, 541–545.

Tuffen, H., Dingwell, D., 2005. Fault textures in volcanic conduits: evidence for seismic trigger mechanism during silicic eruptions. Bull. Volcanol. 67, 370–387.

Voight, B., Sparks, R.S.J., Miller, A.D., Stewart, R.C., Hoblitt, R.P., Clarke, A., Ewart, J., Aspinall, W.P., Baptie, B., Calder, E.S., Cole, P., Druitt, T.H., Hartford, C., Herd, R.A., Jackson, P., Lejeune, A., Lockhart, A.B., Loughlin, S., Luckett, R., Lynch, L., Norton, G.E., Robertson, R., Watson, I.M., Watts, R., Young, S.R., 1999. Magma flow instability and cyclic activity at Soufrière Hills Vocano, Montserrat, British West Indies. Science 283, 1138–1142.

Watson, I.M., Oppenheimer, C., Voight, B., Francis, P., Clarke, A., Stix, J., Miller, A.D., Pyle, D.M., Burton, M.R., Young, S.R., Norton, G.E., Loughlin, S., Darroux, B., Staff, M.V.O., 2000. The relationship between degassing and ground deformation at Soufrière Hills Volcano, Montserrat. J. Volcanol. Geotherm. Res. 98, 117–126.

Westrich, H.R., Eichelberger, J.C., 1994. Gas transport and bubble collapse in rhyolitic magma: an experimental approach. Bull. Volcanol. 56, 447–458.

Wylie, J.J., Voight, B., Whitehead, J.A., 1999. Instability of magma flow from volatile-dependent viscosity. Science 285, 1883–1885.